

Research Article

Coordinated Control of an Islanded Microintegrated Energy System with an Electrolyzer and Micro-Gas Turbine

Huaren Wu 

Institute of Energy Internet, Zhongbei College, Nanjing Normal University, Danyang 212300, China

Correspondence should be addressed to Huaren Wu; 61031@njnu.edu.cn

Received 27 February 2022; Accepted 5 October 2022; Published 26 October 2022

Academic Editor: Jiangbo Yu

Copyright © 2022 Huaren Wu. This is an open access article distributed under the Creative Commons Attribution License, which permits unrestricted use, distribution, and reproduction in any medium, provided the original work is properly cited.

Microintegrated energy systems (MIESs) can be disconnected from power distribution systems during power system faults. This paper develops a control scheme for an islanded MIES. The VSC inverter controls the AC bus voltage and frequency using a modified AC voltage regulator and a modified frequency regulator. The control structures of the power-to-gas and PMSG-based microturbine generator (MTG) systems are improved. Renewable generation always runs at the maximum power point. The surplus renewable energy in the MIES can be converted into natural gas using power-to-gas, and the MIES can make full use of renewable energy. The proposed coordinated control scheme of the electrolyzer and the supercapacitor can achieve a power balance of the islanded MIES and reduce the DC-link voltage fluctuation. A micro-gas turbine can provide electric energy to the load and enhance distribution system resilience. A coordinated control scheme of the MTG and the supercapacitor is developed to improve MIES operation. A feature of this paper is the research on fault ride-through of the islanded MIES. A fault ride-through strategy is proposed, where the AC voltage of the VSC inverter is reduced to limit the short-circuit current during AC system faults. Islanded MIES simulations are conducted in a MATLAB/Simulink environment to test the control scheme. The simulation results verify the effectiveness of the control scheme during normal operation and failure.

1. Introduction

Conventional fossil fuel generation produces carbon dioxide, which is associated with the greenhouse warming of Earth [1]. The emission of sulfur dioxide, nitrogen oxide, particulates, carbon monoxide, hydrocarbons, heat, and other types of radiation from fossil fueled steam-electric generators leads to an increase in the environmental pollution level [2]. In addition, the cost of fossil fuels is gradually increasing. Therefore, renewable energy sources, such as solar and wind, have received considerable attention. Solar energy and wind energy are clean and sustainable energy sources, and solar power generation and wind power generation have found an increasingly wide utilization around the world.

Giroux et al. [3] gave a Simulink model of the grid-connected photovoltaic (PV) system. The PV system uses the “Incremental Conductance + Integral Regulator” technique to control the DC-DC boost converter to implement maximum power point tracking (MPPT). A three-phase

three-level voltage source converter (VSC) in the PV system uses a controller with both the outer DC-link voltage control loop and the inner grid current control loop. Vector control is then used to accomplish decoupling control. A model reference adaptive controller (MRAC) was developed for a grid-connected PV system in [4]. MRACs are designed for both DC-link voltage and grid current control loops. MRACs can improve the performance of the PV system in a low DC-link voltage ripple, with a superior power extraction and improved grid power quality.

A doubly fed induction generator (DFIG) and a permanent magnet synchronous generator (PMSG) are used for wind power generation (WPG). An example in [5] shows a 9 MW wind farm consisting of six DFIGs driven by wind turbines. The rotor of the DFIG is fed at a variable frequency through the grid-side converter and rotor-side converter. The controller of the grid-side converter has both DC voltage and grid current control loops using a PI control. The rotor-side converter is controlled by the electromagnetic

torque controller, the Var/Volt regulator and the current regulator. The electromagnetic torque controller and the Var/Volt regulator generate the references for the current regulator. DFIG technology can track the maximum power point by optimizing the turbine speed. Cortes-Vega et al. described WPG system based on a PMSG and a back-to-back power converter, and proposed optimal controllers for both the generator-side converter and the grid-side converter [6], which can reach a wide system operating range.

Renewable generation is CO₂-free and brings great environmental benefits. However, renewable energy is highly volatile and intermittent [7]. It is difficult to control a power system with a high penetration of intermittent-renewable generation. Energy storage can reduce power fluctuation and improve the operation characteristics of the power system. Batteries and supercapacitors (SCs) are important energy storage devices. Faisal et al. [8] presented a fuzzy controller to control the charging–discharging of the battery. The fuzzy model is based on an ampere-hour technique that is used to evaluate the battery state of charge (SOC). The fuzzy controller schematic is depicted in [8]. The numerical simulations show the effectiveness of the fuzzy controller. MATLAB software provides an example of SC control during charge and discharge [9]. SC is connected to a buck/boost converter. Pulse generators of boost/boost converters are used to obtain an appropriate resolution of PWM waveforms and the current regulator uses PI control. The batteries and SCs can suppress power fluctuations. Control strategies of hybrid energy storage systems (HESS) are reviewed in [10]. Babu et al. [10] presented an implementation of HESS for standalone and grid-connected microgrid systems. Filtration-based control and rule-based control techniques of HESSs are described in [10]. Chen et al. depicted the topology of a three-level bidirectional DC-DC converter for HESSs and proposed a model predictive control (MPC) method to control the converter in [11]. The MPC controller can suppress the DC bus power fluctuations and mitigate power fluctuations in the microgrid.

A microgrid contains an energy storage device, solar power, and/or wind power generation. Alghamdi and Cañizares [12] introduced an adaptive active power droop controller and a voltage setpoint control in isolated microgrids. The controller adopts an optimal and model predictive control approach that continuously adjusts the active power droop gains. The control technique can improve the frequency response of the microgrid and enhance the system's stability [12]. MPC is used to distributed secondary regulation of the frequency and voltage of a microgrid in [13]. A model of a virtual synchronous generator (VSG) and secondary regulation algorithms of frequency and voltage have been described [13]. The control scheme can accurately regulate both the frequency and voltage of microgrids. Babayomi et al. proposed a self-adaptive secondary frequency regulation strategy for a microgrid in [14]. VSG control was applied to renewable energy units, and PI control was introduced into the power-frequency controller of VSGs to achieve zero-error frequency regulation. The secondary frequency regulation parameters of VSGs are adjusted using a self-adaptive strategy.

The surplus renewable energy is curtailed or wasted due to the limited capacity of batteries and SCs. Power-to-gas (P2G) technology can convert electrical energy into natural gas, which can then be injected into natural gas networks. P2G technology is regarded as a long-term, large capacity energy storage solution [15]. P2G technology can realize a high penetration of renewables, a low power fluctuation, and low carbon emissions. Several obvious technological advantages of P2G are described in [16]. The process of electrolyzing water converts electric energy into chemical energy to form hydrogen and oxygen. Under the action of the catalyst, hydrogen and carbon dioxide can react to give water and methane [17]. An electrolyzer is a core facility of a P2G system. Alkaline electrolyzers are commercially available for producing hydrogen using water. Reference [18] developed a mathematical model for an alkaline electrolyzer based on a combination of fundamental thermodynamics, heat transfer theory, and empirical electrochemical relationships. Martinez and Zamora [19] constructed a model of an alkaline electrolyzer using MATLAB/Simulink math blocks. Electrolyzer Simscape power system integration was implemented by utilizing voltage/current controlled source blocks in [19]. Zhou et al. presented a similar model of an alkaline electrolyzer and depicted the control scheme of the hydrogen-production process [20].

Extreme weather events can damage pylons and distribution lines and cause failures of distribution systems [21]. A microgrid can improve the distribution system resilience. However, sequential extreme weather events can lead to outages of the distribution systems for a long period of time. Meanwhile, renewable generation and energy storage cannot supply sufficient power. Natural gas-fired generation would also enhance the resilience of distribution systems. A natural gas pipeline system is usually laid underground and could be less vulnerable to extreme weather events [22]. Hence, gas-fired generation can provide a reliable power supply during extreme weather events. Moreover, gas-fired generation has superior characteristics, such as low pollution, a fast response, and a high efficiency [23]. Rowen presented a model of heavy-duty gas turbines with speed control, temperature control, and acceleration control [24]. Inlet guide vanes (IGVs) in the gas turbine change the geometry in order to regulate the airflow from the compressor. Rowen added IGVs to the original model to include the effect of IGVs on the gas turbine dynamics [25]. Rowen's model is one of most widely used models of gas turbines. Rowen's model is used as a model of a micro-gas turbine in [26, 27]. Yee et al. [28] provided an overview of various gas turbine models published in different studies. Physical models, Rowen's model, the IEEE model, aero-derivative model, GAST model, WECC/GGOV1 model, CIGRE model, and frequency-dependent model of gas turbines are identified, presented, and discussed for system stability studies, especially those for transient and small disturbance stability studies in [28]. Wang and Zheng [29] introduced a control strategy of a PMSG-based microturbine generator (MTG) system connected to a distribution system through an AC-to-DC converter and a DC-to-AC inverter. The inverter is controlled by a damping controller designed using modal control theory. The damping controller can provide effective damping characteristics to the grid-connected MTG system under disturbance conditions.

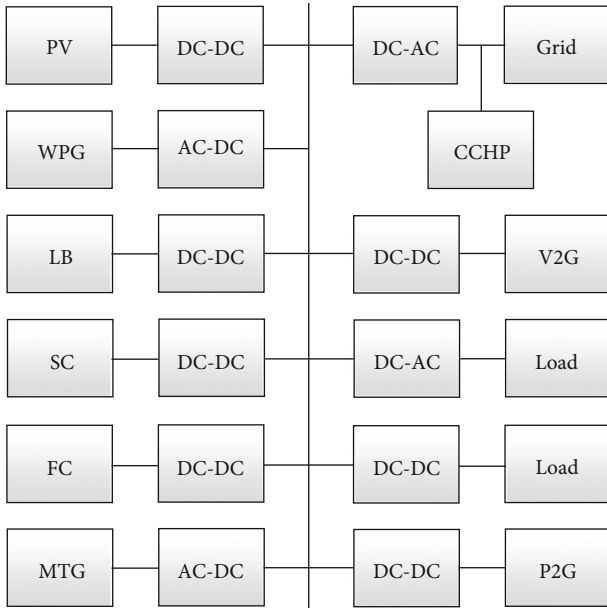


FIGURE 1: MIES structure.

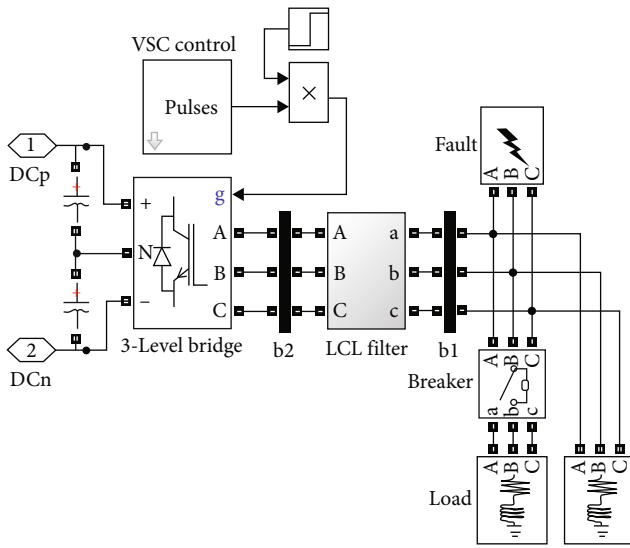


FIGURE 2: AC system consisting of an inverter, LCL filter, and AC load.

Dong et al. [30] described the structure of an integrated energy system (IES). The IES includes PV, wind power generation, energy storage system, P2G, MTG, an electric boiler, and combined heat and power. Ma and He researched the stability control method of a gas-electricity combined system with wind power [31]. The power of the MTG is 250 kW, and the voltage frequency of the generator driven by the microturbine is 50 Hz.

Joshi et al. reviewed the control strategies of PV systems under low-voltage ride-through (LVRT) [32]. The control strategies in the literature are the AC bus voltage support, current limitation, and DC-link voltage control strategies. The control strategies are analyzed under different types of

grid faults. Ren et al. [33] proposed a superconducting magnetic energy storage device, which can suppress the overcurrent under a fault ride through (FRT). The control strategies may be used in the IES under FRT.

The difficulty of IES control lies in the control of DC-DC converters and DC-AC converters. This paper first introduces the models of electrolyzer, gas turbine, and PMSG. Then, the structures and principles of the controller of the VSC inverter, SC, electrolyzer, and MTG are described. The controller performances are then tested by simulations in a MATLAB/Simulink environment.

2. Modeling and Control of MIES

Microintegrated energy system (MIES) may contain PV, WPG, lithium batteries (LB), SC, fuel cell (FC), vehicle-to-grid (V2G), P2G, MTG, AC load, DC load, and combined cooling, heating, and power (CCHP). The power of the device in MIES is in the range from 10 kW to 500 kW. There are many types of MIES structures. Figure 1 shows one of the MIES structures.

Renewable generation in MIES uses the MPPT technique to make full use of renewable energy during normal operation [3, 5]. HESS can be charged or discharged to reduce power fluctuations [9]. If the renewable generation power is greater than the load power, P2G runs to produce natural gas. Otherwise, the MTG generates the electricity to load. This paper studies an MIES consisting of PV, SC, an electrolyzer, MTG, AC load, and DC load. The control schemes of the voltage source inverter, electrolyzer, and MTG are introduced below.

2.1. Control Scheme of the Voltage Source Inverter. There is a voltage source inverter in the MIES. The VSC inverter converts the DC power into AC power. Figure 2 represents the AC system, consisting of an inverter, LCL filter, and AC load.

The fault block in Figure 2 is used to simulate the fault in the AC system and the breaker block to simulate a load fluctuation. The VSC control block generates the signal to control the inverter to maintain a constant AC voltage and frequency of bus b1. The VSC control block is depicted in Figure 3.

Vb1 in Figure 3 is the three-phase AC voltage of bus b1 in Figure 2. The RMS block calculates the RMS of the bus phase voltage. PLL is the frequency measurement block. PI1 in Figure 3 is a bus voltage controller, and PI2 is a frequency controller. Two controllers use PI control technology to realize secondary regulation of the voltage and frequency of bus b1. The $V_{abc.ref}$ block generates the reference value of the three-phase voltage according to the following:

$$\begin{cases} v_a = k_v V_m \sin(\omega t), \\ v_b = k_v V_m \sin(\omega t - 2\pi/3), \\ v_c = k_v V_m \sin(\omega t + 2\pi/3), \end{cases} \quad (1)$$

where $k_v = 2/V_{dc}$ and V_{dc} is the DC-link voltage of the MIES.

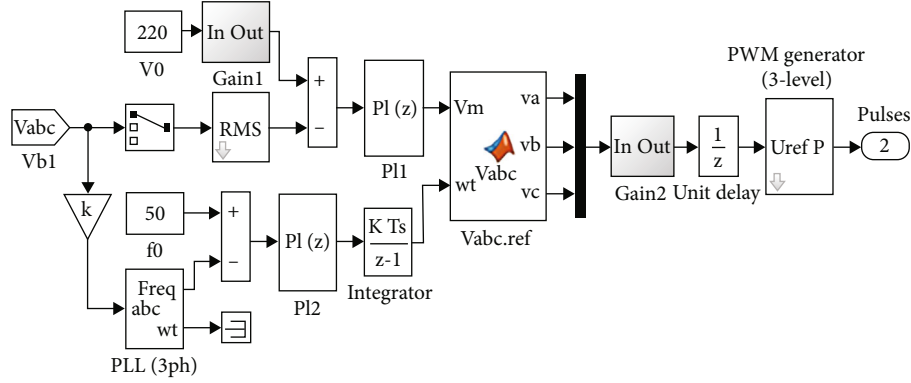


FIGURE 3: VSC control.

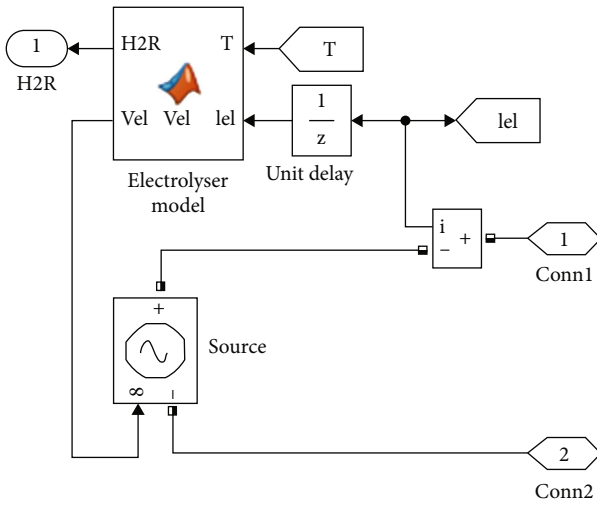


FIGURE 4: Electrolyzer model in MATLAB/Simulink.

The PWM generator block generates a PWM signal to control the 3-level bridge. The Gain1 and Gain2 blocks in Figure 3 are gains to reduce the voltage reference of the fault phase to limit the fault current during a fault.

2.2. Coordinated Control of the Electrolyzer and SC. The PV system in the MIES operates at the maximum power point. If the power of the PV system is greater than the load power, then the MTG is disconnected from the MIES. The MIES is composed of PV, SC, an electrolyzer, a DC load, and an AC load.

Ulleberg proposed a temperature-dependent I-U model of the electrolyzer [18]. If $I \leq 0$, the model in [18] is simplified as $V = V_{rev}$. The temperature-dependent I-U model of the electrolyzer is represented in the following:

$$V = \begin{cases} V_{rev} + \frac{r_1 + r_2 T}{A} I + \log\left(\left(t_1 + \frac{t_2}{T} + \frac{t_3}{T^2}\right) \frac{I}{A} + 1\right) & I > 0, \\ V_{rev} & I \leq 0, \end{cases} \quad (2)$$

where T is the cell temperature, A is the electrode area, and r_1 , r_2 , t_1 , t_2 , t_3 , and s are the overvoltage parameters. V_{rev} is the reversible cell voltage and is considered constant for temperature ranges of up to 100°C [19].

An empirical expression for the production rate of hydrogen is given in the following:

$$\dot{n}\text{H}_2 = \left(\frac{(I/A)^2}{f_1 + (I/A)^2} f_2 \right) \frac{I}{zF}, \quad (3)$$

where \dot{n} is the molar flow rate per second, z is the number of electrons transferred in the reaction, and F is the Faraday constant, and f_1 and f_2 are calculated as follows: [19].

$$\begin{cases} f_1 = 2.5T + 50, \\ f_2 = 1 - 6.24 \times 10^{-6} T^2. \end{cases} \quad (4)$$

The electrolyzer model is represented by (5) for the N_c cells in series.

$$V_{el} = N_c V. \quad (5)$$

Multiple branches of cells are connected in parallel to increase the electrolyzer power. Equations (2)–(5) are algebraic equations and may be computed by the MATLAB function. The controlled voltage source block converts the Simulink input signal into an equivalent voltage source. Figure 4 shows the implementation of the electrolyzer model in MATLAB/Simulink [34]. Iel in Figure 4 is the current of the electrolyzer with multiple branches of cells. H2R in Figure 4 is the production rate of hydrogen.

The DC-link voltage V_{dc} in the MIES is greater than the electrolyzer voltage V_{el} . Therefore, the electrolyzer is connected to the DC bus through a DC-DC buck converter [34]. The DC-DC buck converter and current regulator are displayed in Figure 5. The DC-DC buck converter connects the LCL filter to reduce the harmonics, and the rate limiter limits the slope of the electrolyzer power for electrolyzer security [20]. The electrolyzer current regulator adopts a PI control.

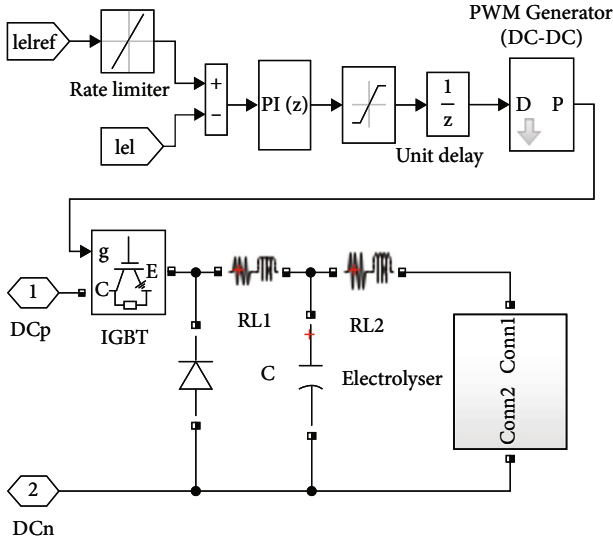


FIGURE 5: DC-DC buck converter and current regulator.

The fluctuation of PV or load power leads to a V_{dc} change. The V_{dc} regulator gives the reference value $I_{el.ref}$ of the electrolyzer current for the power balance of the MIES. The SC current reference $I_{sc.ref}$ is the difference between the current reference $I_{el.ref}$ and the current I_{el} of the electrolyzer. The coordinated control scheme of the electrolyzer and SC is shown in Figure 6.

2.3. Coordinated Control of MTG and SC. If the power of the PV system is less than the load power, then the electrolyzer is disconnected from the MIES. The MIES is composed of PV, SC, MTG, a DC load, and an AC load. MTG provides power to the load and can improve the resilience of distribution systems. Fewer HESSs can be installed due to the MTG. The MTG structure is depicted in Figure 7. An LC filter may be added between the AC-DC converter and PMSG to diminish the harmonics in the stator currents.

The high-speed micro-gas turbine drives PMSG in Figure 7. The 3-level bridge converter transforms the AC power into DC power. The MATLAB PMSG block is used for simulation. The PMSG model is expressed in the following: [35].

$$\frac{d}{dt}i_d = \frac{1}{L_d}v_d - \frac{R}{L_d}i_d + \frac{L_q}{L_d}\omega i_q, \quad (6)$$

$$\frac{d}{dt}i_q = \frac{1}{L_q}v_q - \frac{R}{L_q}i_q - \frac{L_d}{L_q}\omega i_d - \frac{\lambda\omega}{L_q}, \quad (7)$$

$$T_e = 1.5p[\lambda i_q + (L_d - L_q)i_d i_q], \quad (8)$$

where i_d and i_q represent the d- and q-axis currents, respectively, λ is the amplitude of the flux induced by the permanent magnets of the rotor in the stator phases, p is the number of pole pairs, and T_e is the electromagnetic torque. If PMSG is in generator mode, then the mechanical torque $T_m < 0$ and the speed $\omega > 0$.

The d- and q-axis voltages can be obtained from the following:

$$v_d = Ri_d + L_d \frac{d}{dt}i_d - \omega L_q i_q, \quad (9)$$

$$v_q = Ri_q + L_q \frac{d}{dt}i_q + \omega L_d i_d + \lambda\omega. \quad (10)$$

The control block of the AC-DC converter in Figure 7 uses the control algorithms represented in the following:

$$v_d = Ri_d + \left(k_p + \frac{k_i}{s}\right)(i_{d.ref} - i_d) - \omega L_q i_q, \quad (11)$$

$$v_q = Ri_q + \left(k_p + \frac{k_i}{s}\right)(i_{q.ref} - i_q) + \omega L_d i_d + \lambda\omega, \quad (12)$$

where $i_{d.ref}$ and $i_{q.ref}$ are the d- and q-axis current references, respectively, and $i_{d.ref} = 0$.

Three-phase sinusoidal voltages are computed using v_d , v_q , and the rotor angle, and then PWM pulses are generated for AC-DC converter control.

Rowen's model of a gas turbine is shown in Figure 8 [24, 26]. Rowen's model includes a compressor-turbine model, a speed controller, an acceleration controller, a fuel controller, and temperature controller [26]. Equations f_1 and f_2 in Figure 8 are given as follows [24]:

$$f_1 = T_R - 700(1 - W_{f1}) + 550(1 - N), \quad (13)$$

$$f_2 = 1.3(W_{f2} - 0.23) + 0.5(1 - N), \quad (14)$$

where N is the rotor speed per unit.

The current reference $i_{q.ref}$ in (12) is given by the V_{dc} voltage regulator in Figure 9. The rate limiter limits the slope of the current $i_{q.ref}$ to improve the operating conditions of the micro-gas turbine.

3. Simulation Results

Simulations of islanded MIES are performed in the MATLAB/Simulink environment to assess the performance of the above controllers. The scheme of islanded MIES is shown in Figure 1. The DC-link voltage reference $V_{dc.ref}$ of the MIES is 780 V, the normal voltage of the AC bus is 380 V, and the frequency is 50 Hz. There are two PV arrays in the MIES. Each PV array delivers a maximum of 140 kW at a 1000 W/m² sun irradiance. PV arrays always run in MPPT control to make full use of renewable energy. MPPT control of PV arrays is introduced in [3]. The rated voltage of the SC is 250 V, and the SC controller is represented in [9]. The rated power of the VSC inverter is 300 kW, and its controller is depicted in Figure 3. The proportional gain k_p and the integral gain k_i of the voltage regulator in Figure 3 are 1 and 10, respectively, while k_p and k_i of the frequency regulator are 0.1 and 1, respectively.

3.1. Coordinated Control of the Electrolyzer, SC, and VSC Inverter. The output power of the two PV arrays is 280 kW

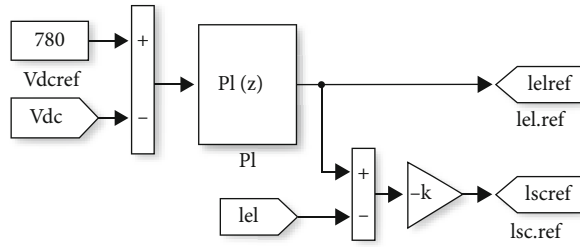


FIGURE 6: Coordinated control scheme of the electrolyzer and SC.

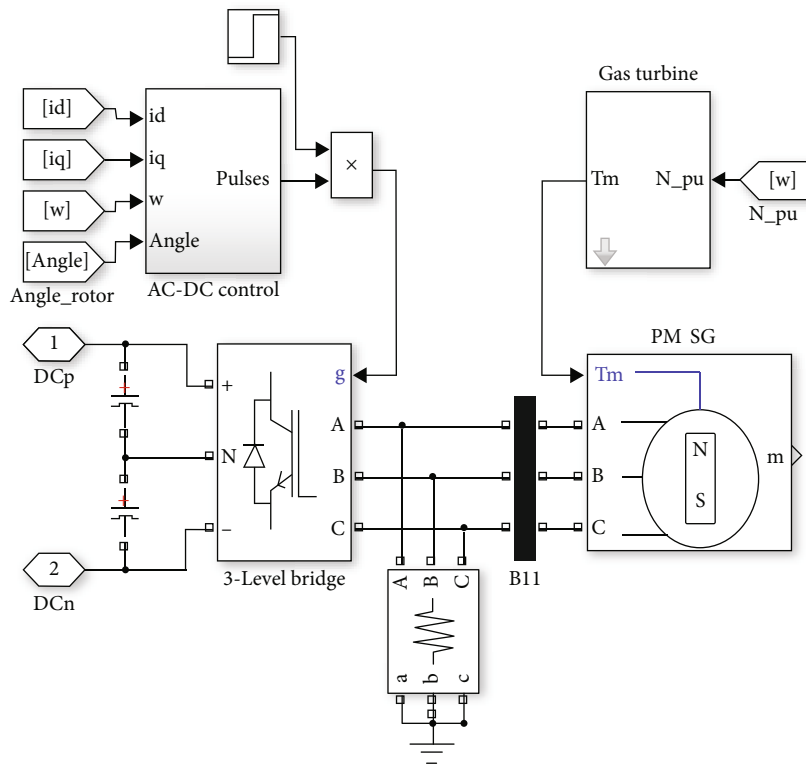


FIGURE 7: MTG structure.

because the sun irradiance reaches 1000 W/m^2 . The DC load is 50 kW , and the AC load is $100 + j50 \text{ kVA}$. The output power of the two PV arrays is greater than the load power. The surplus PV energy is converted into hydrogen by an electrolyzer. Islanded MIES is composed of two PV arrays, an SC, VSC inverter, a DC load, an AC load, and an electrolyzer. The parameters in (2) and (3) are given in [19, 34]. N_C in (5) is 120. The electrolyzer has 100 branches of cells in

parallel. The parameters of the controller in Figure 5 are $k_p = 0.5$ and $k_i = 1$. The current references $I_{el.ref}$ and $I_{sc.ref}$ of the electrolyzer and SC are provided by the control system shown in Figure 6. The parameters of the controller in Figure 6 are $k_p = 5$ and $k_i = 20$.

3.1.1. AC Load Changes. The controller performances are tested by AC load changing. The AC load increases by 50

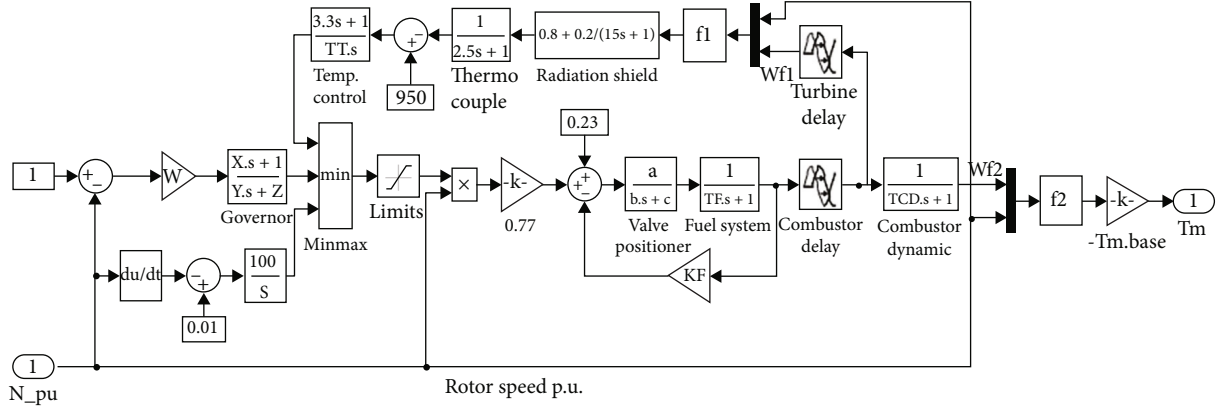


FIGURE 8: Rowen's model of a gas turbine.

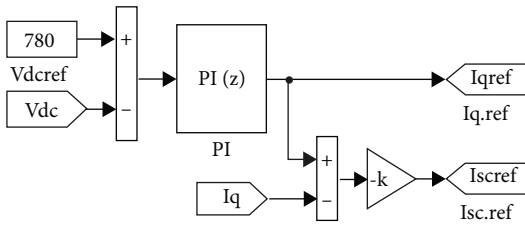


FIGURE 9: Coordinated control scheme of the AC-DC rectifier and SC.

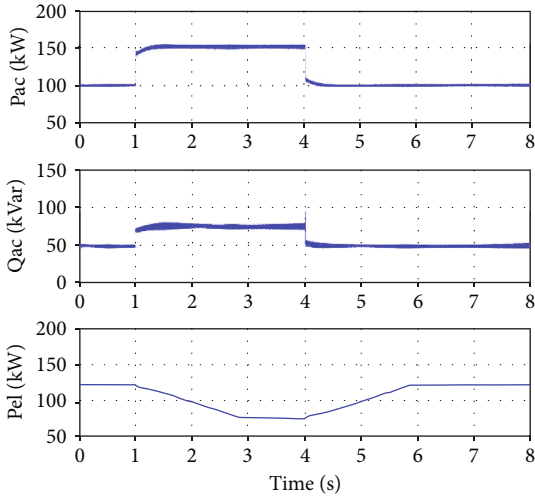


FIGURE 10: AC load and electrolyzer power during an AC load change.

+ j25 kVA from $t = 1$ s to 4 s. The SC and electrolyzer power must be regulated for the power balance of islanded MIES. Figure 10 shows the AC load P_{ac} , Q_{ac} , and electrolyzer power P_{el} . The SC power P_{sc} , DC-link voltage V_{dc} , and AC bus voltage V_{ac} are shown in Figure 11. The electrolyzer power gradually decreases at $t = 1$ s and increases at $t = 4$ s because of the function of the rate limiter. The power delivered by SC increases quickly at $t = 1$ s and decreases at $t = 4$ s. The maximum deviation from the voltage reference $V_{dc,ref}$ is 3.9%

during the AC load change. The maximum deviation from the voltage reference of V_{ac} is 4.6%. The coordinated control of the electrolyzer, SC, and VSC inverter has a good performance during AC load change.

3.1.2. AC Bus Fault. The controller performances are tested during an AC bus fault. The three-phase fault block in Simulink is connected in bus b1 at $t = 0.2$ s. The fault is identified at $t = 0.20093$ s, and then Gain1 and Gain2 are changed from 1 to 0.2 to limit the short-circuit current. The fault is cleared at $t = 0.4$ s, and then Gain1 and Gain2 increase gradually from 0.2 to 1. The output power of the VSC inverter decreases during an AC bus fault. Therefore, the electrolyzer power P_{el} increases, and the SC absorbs power for a power balance. The AC bus voltages $V_{abc,b1}$, the electrolyzer power P_{el} and the SC power P_{sc} are exhibited in Figure 12. Figure 13 shows the DC-link voltage V_{dc} and the three-phase currents $I_{abc,b2}$ flowing through bus b2 in Figure 2. The maximum deviation of V_{dc} is 5.9% during an AC bus fault. The currents $I_{abc,b2}$ are less than 124% of the rated current amplitude of the VSC inverter. The proposed control strategies satisfy the control requirements.

3.2. Coordinated Control of the MTG, SC, and VSC Inverters. The output power of the two PV arrays is 140 kW. The DC load is 100 kW, and the AC load is $210 + j80$ kVA. PV powers are less than the load power. The electrolyzer is disconnected from the MIES, and MTG provides power to loads. The islanded MIES is composed of two PV arrays, SC, VSC inverter, a DC load, an AC load, and MTG. Figure 7 shows the MTG system. The rated voltage, frequency, and power of the high-speed PMSG are 380 V, 1000 Hz, and 300 kW, respectively. The gas turbine model is described in Figure 8. The model parameters of the gas turbine are given in reference [24]. The controller of the AC-DC rectifier in MTG is constituted on the basis of (11) and (12).

The parameters k_p and k_i in (11) and (12) are 1 and 2, respectively. The current references $I_{q,ref}$ and $I_{sc,ref}$ are provided by the control system shown in Figure 9. The controller parameters k_p and k_i in Figure 9 are 20 and 100, respectively. The step size in the simulation should not be greater than 0.0000001.

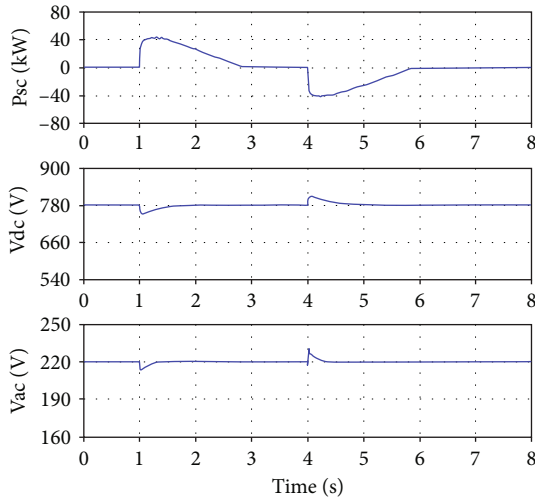


FIGURE 11: SC power, DC-link voltage, and AC bus voltage during an AC load change.

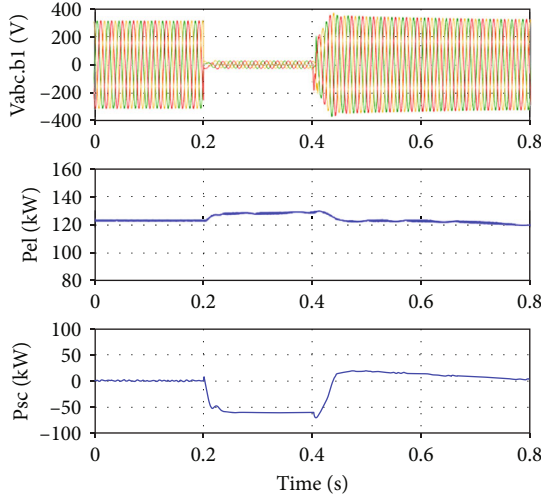


FIGURE 12: AC bus voltages, electrolyzer power, and SC power during an AC bus fault.

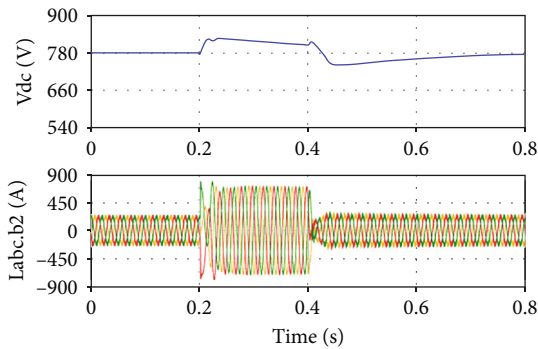


FIGURE 13: DC-link voltage and inverter currents during an AC bus fault.

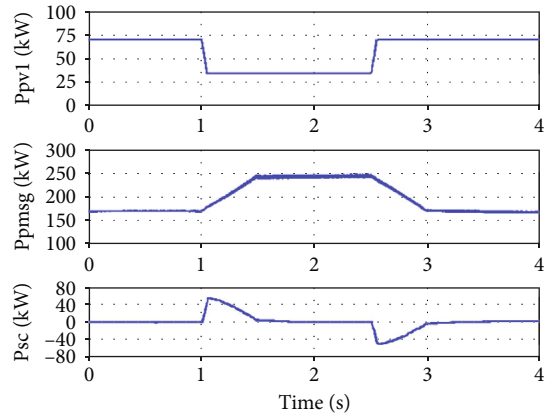


FIGURE 14: Output powers of a PV array, MTG, and SC during irradiance changes.

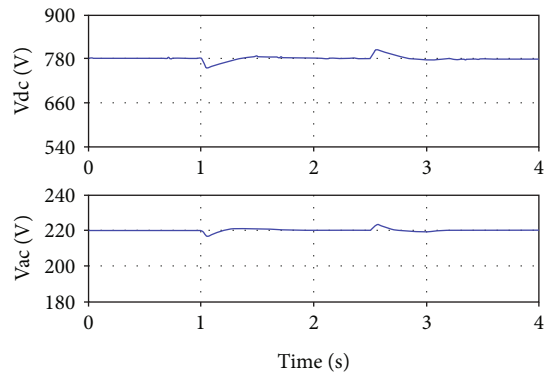


FIGURE 15: DC-link voltage and AC bus voltage during irradiance changes.

3.2.1. *Irradiance Changes.* The PV output power changes if the irradiance or temperature changes; hence, the MTG and SC power must be regulated for the power balance of islanded MIES. The controllers are tested for adapting to PV power changes. Figure 14 shows the output powers of a PV array, MTG and SC, and the DC-link voltage and AC bus voltage are shown in Figure 15. The output power of the two PV arrays decreases from 140 kW to 70 kW between 1 s and 2.5 s, while MTG power increases from 170 kW to 240 kW, and SC power changes quickly for power balance. The maximum deviation of V_{dc} is 3.5% between 1 s and 2.5 s. The voltage regulator in Figure 3 controls the inverter output voltage. The maximum deviation of the bus voltage V_{ac} is 1.6%. The above controllers can effectively control the islanded MIES when PV power changes.

3.2.2. *Fault Ride-through.* The AC bus fault is applied between 0.2 s and 0.4 s to test the above controller performances. Two PV arrays always run in MPPT control and provide 140 kW. The fault is identified at $t = 0.20065$ s, and then Gain1 and Gain2 are changed from 1 to 0.2. Gain1 and Gain2 gradually increase from 0.2 to 1 at $t = 0.4$ s. The AC bus voltages $V_{abc,b1}$, MTG power P_{pmsg} , and SC power P_{sc} are described in Figure 16, and the DC-link voltage V_{dc}

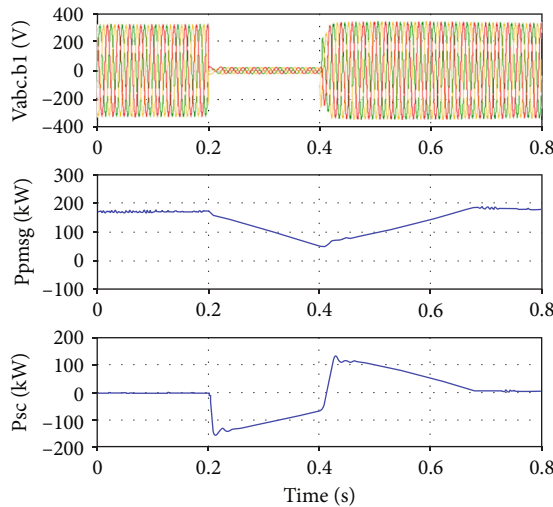


FIGURE 16: AC bus voltages, MTG power, and SC power during FRT.

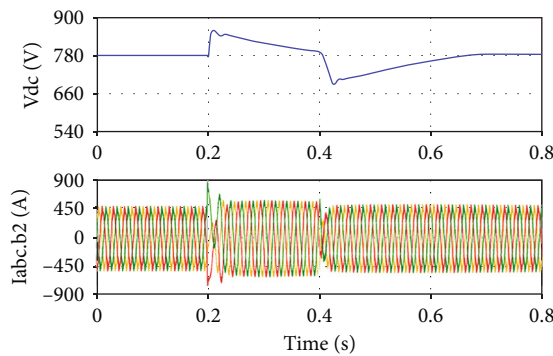


FIGURE 17: DC-link voltage and the three-phase currents during FRT.

and the three-phase currents $I_{abc.b2}$ are represented in Figure 17. MTG power changes continuously between 0.2 s and 0.4 s, while SC power changes quickly to reduce the DC-link voltage deviation.

The maximum deviation of V_{dc} is 11.8% during an AC bus fault. The currents $I_{abc.b2}$ are less than 135.2% of the rated current amplitude of the VSC inverter. The proposed coordinated control scheme of the MTG, SC and VSC inverters has good performance during AC bus faults.

4. Conclusion

An islanded MIES is an important operation mode, and the coordinated control of an islanded MIES was studied in this paper. The developed coordinated control scheme of an islanded MIES can properly distribute the power among the electrolyzer, MTG, and supercapacitor on the basis of their characteristics. The proposed current regulator of the electrolyzer can stably control the power of the electrolyzer according to the power given by the coordinated control systems of the islanded MIES. The improved control system of

the AC-DC rectifier of the MTG can robustly control the power of the AC-DC rectifier according to the given power. The suggested control methods can achieve a power balance in islanded MIESs and diminish the fluctuations of DC-link voltage, AC bus voltage, and frequency in disturbance. Renewable generation in an MIES can always operate in MPPT mode and replace fossil energy to the greatest extent possible to reduce pollution and CO₂ emissions. The MTG can provide power to loads and enhance MIES resilience when the output power of renewable generation is insufficient.

The control methods of the VSC inverter are improved. The AC voltages of the VSC inverter are reduced during AC bus faults and gradually increase after fault removal. The suggested control methods can thereby limit the short-circuit current and effectively control the SC, electrolyzer, and MTG systems during AC bus faults.

Models of an electrolyzer, high-speed micro-gas turbine, and PMSG were tested during normal operation and failure. The models of the electrolyzer and MTG used in this paper can be used for MIES simulations.

Data Availability

The data used to support the findings of this study are included within the article.

Conflicts of Interest

The author declares that there are no conflicts of interest regarding the publication of this paper.

Acknowledgments

This work was financially supported by Zhongbei College, Nanjing Normal University (2021yky006).

References

- [1] A. H. M. Sadrul Ula, "Global warming and electric power generation: what is the connection?," *Energy Conversion*, vol. 6, no. 4, pp. 599–604, 1991.
- [2] K.-C. Chu, M. Jamshidi, and R. E. Levitan, "An approach to on-line power dispatch with ambient air pollution constraints," *IEEE Transactions on Automatic Control*, vol. 22, no. 3, pp. 385–396, 1977.
- [3] P. Giroux, G. Sybille, C. Osorio, and S. Chandrachood, *Detailed model of a 100-kW grid-connected PV array*, MathWorks, Natick, MA, 1977, <https://www.mathworks.com/help/physmod/sps/ug/detailed-model-of-a-100-kw-grid-connected-pv-array.html>.
- [4] M. Bhunia, B. Subudhi, and P. K. Ray, "Design and real-time implementation of cascaded model reference adaptive controllers for a three-phase grid-connected PV system," *IEEE Journal of Photovoltaics*, vol. 11, no. 5, pp. 1319–1331, 2021.
- [5] R. Gagnon, *Wind farm-DFIG detailed model*, MathWorks, Natick, MA, 2007, <https://www.mathworks.com/help/releases/R2016b/physmod/sps/examples/wind-farm-dfig-detailed-model.html>.

- [6] D. Cortes-Vega, F. Ornelas-Tellez, and J. Anzures-Marin, "Nonlinear optimal control for PMSG-based wind energy conversion systems," *IEEE Latin America Transactions*, vol. 19, no. 7, pp. 1191–1198, 2021.
- [7] P. Shinde, M. R. Hesamzadeh, P. Date, and D. W. Bunn, "Optimal dispatch in a balancing market with intermittent renewable generation," *IEEE Transactions on Power Systems*, vol. 36, no. 2, pp. 865–878, 2021.
- [8] M. Faisal, M. A. Hannan, P. J. Ker, M. S. H. Lipu, and M. N. Uddin, "Fuzzy-based charging–discharging controller for lithium-ion battery in microgrid applications," *IEEE Transactions on Industry Applications*, vol. 57, no. 4, pp. 4187–4195, 2021.
- [9] P. C. Blaud and L.-A. Dessaint, *Supercapacitor model*, MathWorks, Natick, MA, 2011, <https://ww2.mathworks.cn/help/physmod/sps/ug/supercapacitor-model.html>.
- [10] T. S. Babu, K. R. Vasudevan, V. K. Ramachandaramurthy, S. B. Sani, S. Chemud, and R. M. Lajim, "A comprehensive review of hybrid energy storage systems: converter topologies, control strategies and future prospects," *IEEE Access*, vol. 8, pp. 148702–148721, 2020.
- [11] S. Chen, Q. Yang, J. Zhou, and X. Chen, "A model predictive control method for hybrid energy storage systems," *CSEE Journal of Power and Energy Systems*, vol. 7, no. 2, pp. 329–338, 2021.
- [12] B. Alghamdi and C. A. Cañizares, "Frequency regulation in isolated microgrids through optimal droop gain and voltage control," *IEEE Transactions on Smart Grid*, vol. 12, no. 2, pp. 988–998, 2021.
- [13] Q. Zhang, Y. Li, Z. Ding, W. Xie, and C. Li, "Self-adaptive secondary frequency regulation strategy of micro-grid with multiple virtual synchronous generators," *IEEE Transactions on Industry Applications*, vol. 56, no. 5, pp. 6007–6018, 2020.
- [14] O. Babayomi, Z. Li, and Z. Zhang, "Distributed secondary frequency and voltage control of parallel-connected VSCs in microgrids: a predictive VSG-based solution," *CPSS Transactions on Power Electronics and Applications*, vol. 5, no. 4, pp. 342–351, 2020.
- [15] R. Zhang, T. Jiang, F. Li, G. Li, H. Chen, and X. Li, "Coordinated bidding strategy of wind farms and power-to-gas facilities using a cooperative game approach," *IEEE Transactions on Sustainable Energy*, vol. 11, no. 4, pp. 2545–2555, 2020.
- [16] X. Xing, J. Lin, Y. Song, Y. Zhou, S. Mu, and Q. Hu, "Modeling and operation of the power-to-gas system for renewables integration: a review," *CSEE Journal of Power and Energy Systems*, vol. 4, no. 2, pp. 168–178, 2018.
- [17] Y. Jiang and L. Guo, "Research on wind power accommodation for an electricity-heat-gas integrated microgrid system with power-to-gas," *IEEE Access*, vol. 7, pp. 87118–87126, 2019.
- [18] O. Ulleberg, "Modeling of advanced alkaline electrolyzers: a system simulation approach," *International Journal of Hydrogen Energy*, vol. 28, no. 1, pp. 21–33, 2003.
- [19] D. Martinez and R. Zamora, "MATLAB Simscape model of an alkaline electrolyser and its simulation with a directly coupled PV module for Auckland solar irradiance profile," *International Journal of Renewable Energy Research*, vol. 8, pp. 552–560, 2018.
- [20] T. Zhou, B. Francois, M. H. Lebbal, and S. Lecoeuche, "Real-time emulation of a hydrogen-production process for assessment of an active wind-energy conversion system," *IEEE Transactions on Industrial Electronics*, vol. 56, no. 3, pp. 737–746, 2009.
- [21] Y. Shen, C. Gu, Z. Ma, X. Yang, and P. Zhao, "A two-stage resilience enhancement for distribution systems under hurricane attacks," *IEEE Systems Journal*, vol. 15, no. 1, pp. 653–661, 2021.
- [22] C. Shao, M. Shahidehpour, X. Wang, X. Wang, and B. Wang, "Integrated planning of electricity and natural gas transportation systems for enhancing the power grid resilience," *IEEE Transaction on Power Systems*, vol. 32, no. 6, pp. 4418–4429, 2017.
- [23] R. Liu, S. Lei, C. Peng, W. Sun, and Y. Hou, "Data-based resilience enhancement strategies for electric-gas systems against sequential extreme weather events," *IEEE Transactions on Smart Grid*, vol. 11, no. 6, pp. 5383–5395, 2020.
- [24] W. I. Rowen, "Simplified mathematical representations of heavy-duty gas turbines," *ASME Journal Engineering Power*, vol. 105, no. 4, pp. 865–869, 1983.
- [25] W. I. Rowen, "Simplified mathematical representations of single shaft gas turbines in mechanical drive service," Gas Turbine and Aeroengine Congr. and Expo, Cologne, Germany, 1992.
- [26] S. R. Guda, C. Wang, and M. H. Nehrir, "Modeling of micro-turbine power generation systems," *Electric Power Components and Systems*, vol. 34, no. 9, pp. 1027–1041, 2006.
- [27] A. Hasanzadeh, C. S. Edrington, N. Stroupe, and T. Bevis, "Real-time emulation of a high-speed microturbine permanent-magnet synchronous generator using multiplatform hardware-in-the-loop realization," *IEEE Transaction on Industrial Electronics*, vol. 61, no. 6, pp. 3109–3118, 2014.
- [28] S. K. Yee, J. V. Milanovic, and F. M. Hughes, "Overview and comparative analysis of gas turbine models for system stability studies," *IEEE Transactions on Power Apparatus and Systems*, vol. 23, no. 1, pp. 108–118, 2008.
- [29] L. Wang and G.-Z. Zheng, "Analysis of a microturbine generator system connected to a distribution system through power-electronics converters," *IEEE Transactions on Sustainable Energy*, vol. 2, no. 2, p. 159, 2011.
- [30] J. Dong, H. Wang, J. Yang, X. Lu, L. Gao, and X. Zhou, "Optimal scheduling framework of electricity-gas-heat integrated energy system based on asynchronous advantage actor-critic algorithm," *IEEE Access*, vol. 9, pp. 139685–139696, 2021.
- [31] R. Ma and P. He, "Dynamic modeling gas-electricity combined system with wind power and its stability control method," *CSEE Journal of Power and Energy Systems, Early Access Article*, 2020.
- [32] J. Joshi, A. K. Swami, V. Jatly, and B. Azzopardi, "A comprehensive review of control strategies to overcome challenges during LVRT in PV systems," *IEEE Access*, vol. 9, pp. 121804–121834, 2021.
- [33] J. Ren, X. Xiao, Z. Zheng, and Z. Ma, "A SMES-based dynamic current limiter to improve the LVRT capability of DFIG-based WECS," *IEEE Transactions on Applied Superconductivity*, vol. 31, no. 8, pp. 5401805–5401805, 2021.
- [34] D. Martinez and R. Zamora, "Electrical implementations of an empirical electrolyser model for improved MATLAB/Simulink simulations," *International Journal of Renewable Energy Research*, vol. 9, no. 2, 2019.
- [35] MathWorks, *Permanent Magnet Synchronous Machine*, MathWorks, Natick, MA, 2006, https://www.mathworks.com/help/physmod/sps/powersys/ref/permanent_magnetsynchronousmachine.html.